Microporous and Mesoporous Materials 183 (2014) 81–90

Contents lists available at ScienceDirect

Microporous and Mesoporous Materials

journal homepage: www.elsevier.com/locate/micromeso

Influence of trace elements on the textural properties of synthetic chrysotile: Complementary insights from macroscopic and nanoscopic measurements

Romain Lafay [a,*], German Montes-Hernandez [a,*], Emilie Janots [a], Anne-Line Auzende [b], Rodica Chiriac [c], Damien Lemarchand [d], François Toche [c]

[a] Institut des Sciences de la Terre (ISTerre), UJF-CNRS, F-38041 Grenoble Cedex 9, France
[b] Institut de minéralogie et de physique des milieux condensés (IMPMC), CNRS-UPD-UPMC, 4 place Jussieu, 75252 Paris, France
[c] Laboratoire des Multimatériaux et Interfaces, UMR CNRS 5615, 43 bd du 11 novembre 1918, 69622 Villeurbanne Cedex, France
[d] Laboratoire d'Hydrologie et de GEochimie de Strasbourg (LHyGeS), UMR7517 CNRS, Strasbourg Cedex, France

ARTICLE INFO

Article history:
Received 4 April 2013
Received in revised form 30 July 2013
Accepted 14 August 2013
Available online 5 September 2013

Keywords:
Chrysotile
Trace element
Sequestration
Textural properties
Nanotubes

ABSTRACT

The present study shows that the presence of Li, Sb, As and B as trace elements significantly influences textural properties such as particle size distribution, morphology and specific surface area of chrysotile synthesized under hydrothermal conditions ($P = 8.2$ MPa, $T = 300$ °C and high-alkaline pH (13.5)). Conversely, traces of Cs did not have any textural effect under these conditions. Furthermore, chrysotile nanotubes size and morphology depend strongly on the element considered. Indeed, large chrysotile with cylinder in cylinder morphology (outer diameter up to 50 nm) precipitated in the presence of Li, Sb and As. This implies lower specific surface area (124–160 $m^2 g^{-1}$) compared to undoped chrysotile (184 $m^2 g^{-1}$ with about 14 nm in width). The presence of boron favors the precipitation of thin fibrous nanotubes similar to undoped chrysotile in width, but significantly longer, with tubes length that can reach three microns in length. In this case, the specific surface area increase slightly from 184 to 196 m^2/g. The solid–liquid partition coefficient for each investigated trace element was determined using Langmuir equation. This well-tubular geo-material can be used as a model to better understand the effects of trace elements on the precipitation of minerals that are relevant in Earth systems (e.g., serpentinization processes) and societal applications (e.g., asbestos toxicity and CO_2 sequestration).

1. Introduction

The formation and textural properties of serpentines (i.e., chrysotile, lizardite and antigorite) have already been investigated in the past. However, various questions still remain unanswered, especially concerning their crystallization in natural and experimental systems and the textural effects of foreign ions during their formation was hardly investigated. Chrysotile is made of a succession of concentric or spiral layers with a fivefold symmetry [1–3] forming a nanometric tubular structure with several polymorphs [4–7]. Beyond a critical size (width >100 nm) chrysotile becomes unstable and polygonal serpentine is observed [8,9]. The complexity of chrysotile fibrils structure and morphology makes careful experimental work and nanoscale investigation absolutely essential. Serpentine has been experimentally synthesized for decades [10,11]. Authors were especially interested in the kinetics and stability domains of serpentine polymorphs (lizardite, chrysotile and antigorite) [12,13]. Recently, new experimental protocols have been developed for synthesizing pure homogeneous chrysotile [13–15] and it has become possible to properly investigate the effects of physico-chemical parameters on various properties (texture, thermal stability, kinetics) of chrysotile. These effects are of prime importance since the textural properties (size, morphology, specific surface area) largely influence the reactivity of chrysotile [14,15]. Optimal synthesis protocols have been set up to study health hazards of asbestos mineral [15,16]. Chrysotile synthesis is favored for a high pH (>13) and temperatures between 300 and 400 °C [17,18]. The longest chrysotile nanotubes are formed around 400 °C after 168 h of reaction [17] and the highest chrysotile crystallinity is obtained at pH > 13 in NaOH medium which promotes the incorporation of –OH [18] or using mineralizing agents [19]. Results indicated that synthetic chrysotiles rarely exceed 30 micrometers in length [20] whereas natural chrysotile fibers showed lengths ranging from few nanometers to several centimeters [4,21]. The influence of Mg-substitution has also been investigated to characterize the role of major (Fe) and minor (Ni, Ti,

* Corresponding authors. Tel.: +33(0)4 76 51 40 57.
E-mail addresses: romain.lafay@ujf-grenoble.fr (R. Lafay), german.montes-hernandez@obs.ujf-grenoble.fr (G. Montes-Hernandez).

1387-1811/$ - see front matter © 2013 Elsevier Inc. All rights reserved.
http://dx.doi.org/10.1016/j.micromeso.2013.08.032

Co) elements on the thermal and textural properties of synthetic chrysotile (size and morphology) and on the kinetics of chrysotile formation [16,22].

Both cationic substitution and the presence of impurities have direct implications on atomic bonds and affect the unit-cell geometric parameters of crystals. Consequently, previous studies have indicated that chrysotile nucleation and growth is strongly affected by the presence of major or minor elements (e.g., Fe, Ni, Co) in solution [23–26]. This induces the precipitation of chrysotile particles with complex cylinder in cylinder [27,28], cone-in-cone [25] and/or spiral morphology [29]. Chrysotile synthesized in the presence of Fe-doped solution has a lower thermal stability [22] and faster formation kinetics [30]. Nanotube cores have diameters of about 5–8 nm [31] and a previous study indicated that this particular geometry could favor the sequestration of trace elements such as Li in the hollow center of the nanotubes [32]. Serpentine is an important carrier of fluid mobile elements (e.g., Li, B, Sb, As, Cs, Sr, Pb) in natural settings [33,34]. Thus, understanding the sequestration of these trace-elements during serpentine formation is necessary and can be achieved by experimentation. In the same way, it is important to clearly identify the influence of single- and multi-element systems on the macroscopic and nanoscopic properties of chrysotile. For that purpose, an experimental investigation is crucial to quantify single trace element partitioning during chrysotile precipitation and evaluate the resulting influence of each element on the chrysotile textural properties at all scales.

We based our approach on a published protocol for undoped synthesis ($Mg_3Si_2O_5(OH)_4$) [35]. Trace-element-doped chrysotiles were then synthesized by alternatively adding Li, As, B, Sb or Cs at different concentrations. We estimate that the chemical compositions of the synthetic solids are in equilibrium with the solution after 30 h of reaction. Our goal is twofold. We first determine the effects of the above-mentioned trace elements on the textural properties of chrysotile and then provide new data on the partitioning of trace elements between fluid and solid during chrysotile formation. Geochemical measurements on bulk solid product were carried out using Inductively Coupled Plasma Mass Spectrometry (ICP-MS). Chrysotile products were characterized from macroscopic to nanoscopic scale by performing N_2 adsorption isotherms measurements, ThermoGravimetric Analyses (TGA/SDTA), Field Emission Gun Scanning Electron Microscopy (FESEM) and Transmission Electron Microscopy (TEM).

2. Methods

2.1. Chrysotile synthesis

Syntheses of chrysotile doped with a single trace element were performed using 1.302 g of commercial silica gel (H_2SiO_3 provided by ROTH) and 5.082 g of magnesium chloride hexahydrate ($MgCl_2 \cdot 6H_2O$ provided by ROTH) used without any treatment and mixed in 250 ml of 1 M NaOH solution doped with one single trace element at various concentrations placed in a *Parr copper alloy* reactor (autoclave with internal volume of 0.5 L). The trace element concentrations experienced were 5, 20, 50, 100, 200 $\mu g\ g^{-1}$ for Li, Sb, Cs, B and As elements, and 500 and 1000 $\mu g\ g^{-1}$ in addition for As. This aqueous reactive system was immediately stirred using constant mechanical agitation (300 rpm) during the reaction. The aqueous system was then heated at 300 °C for 30 h using a heating jacket adapted to the reactor, following preliminary experiments on chrysotile syntheses.

At the end of each experiment, the autoclave was removed from the heating system and immersed in cold water. After water cooling down to 30 °C (about 15 min) the autoclave was disassembled, and the solid product was carefully recovered and separated by centrifugation (20 min at 11,500 rpm), decanting the supernatant solutions. The solid product was washed two times by re-dispersion/centrifugation processes in order to remove soluble compounds (e.g.. NaCl and Na_2CO_3) co-formed during synthesis and adsorbed trace elements. Finally, the solid product was dried 90 °C for 48 h and preserved in dry environment for further characterizations (TGA, N_2 adsorption isotherms, FESEM and TEM).

2.2. Analytical procedure

2.2.1. N_2 sorption isotherms

N_2 sorption isotherms were performed for several runs using a Micrometrics ASAP 2010 system. The specific surface area for 100 mg of powdered samples was estimated from the Brunauer–Emmet–Teller (BET) equation in the $0.05 \leqslant P/P_0 \leqslant 0.35$ interval of relative pressure and using 16.2 $Å^2$ for cross-sectional area of molecular N_2. Additionally, the Barrett, Joyner, and Halenda (BJH) method [36] taking into account the capillary condensation using the Kelvin equation was used for the determination of the pore size distribution.

2.2.2. FESEM and TEM observations

Micro-imaging was carried out on a Zeiss Ultra 55 Field Emission gun Scanning Electron Microscopy (FESEM) in order to evaluate the serpentine grain size and morphology. The spatial resolution is approximately 1 nm at 15 kV. Solid samples were dispersed by ultrasonic treatment in absolute ethanol for at least 5 min in order to disaggregate the particles. One or two drops of solution were placed on an aluminum support and coated with a thin film of platinum for SEM observation. Additionally, our samples were scattered for short times in ethanol in order to split the aggregates without any additional treatment. An ethanol drop of the chrysotile suspension was deposited on a holey carbon foil placed on conventional copper micro-grids for further observations with JEOL 2100F Transmission Electron Microscope (TEM) operating at 200 kV, equipped with a field emission gun and a high-resolution pole piece achieving a point-to-point resolution of 1.8 Å. Chemical mapping was achieved by combining the scanning module of the microscope (STEM) to the EDS detector. To try and resolve trace elements, acquisitions were conducted for more than two hours. None of the investigated trace elements were detected by EDS in serpentine, but we were able to resolve the occurrence of oxide precipitation containing high amounts of these elements.

2.2.3. Thermogravimetric analyses (TGA)

TGA for experimental solid products was performed with a TGA/SDTA 851^e Mettler Toledo instrument under the following conditions: sample mass of about 10 mg, platinum crucible of 150 µl with a pinhole, heating rate of 10 °C min^{-1}, and inert N_2 atmosphere of 50 ml min^{-1}. Sample mass loss and associated thermal effects were obtained by TGA/DTGA in a temperature range of 30–1200 °C with an accuracy of about ±0.25 °C.

The melting points of three compounds (indium, aluminum and copper) obtained from the DTGA signals were used for sample temperature calibration. Calcium oxalate was used for mass sample calibration. Weighting accuracy is 0.1 µg, which correspond to 0.01% for a 10 mg sample.

2.2.4. Trace element concentrations measurements

Li concentrations were determined at the Laboratoire d'Hydrologie et de GEochimie de Strasbourg (LHyGeS) by ICP-MS using a Thermo Finnigan X series II. Sb, As and Cs were determined by ICP-MS using an Agilent 7500ce at ISTerre laboratory (Grenoble, France). For Li, about 150 mg of sample was crushed in an agate ring mill before acid digestion by HF and HNO_3. The complete analytical procedure is described in [37]. The same procedure, using

10 mg of sample instead of 150 mg, was applied for the determination of Sb, As and Cs concentration. The precision and accuracy of the ICP-MS analyses were assessed by repeated analyses of three rock standards: serpentinite UBN, basalts BR-24 and BCR-2. Our results show good agreement between measured and certified values for these international references materials [38,39]. To assess the accuracy of Li, Cs, Sb and As, we prepared three artificial standards with a concentration in each trace element of 50 ng g^{-1}, 10 ng g^{-1} and 0.1 ng g^{-1}, respectively in a matrix of 1 μg/g in Si and Mg. Linear regressions obtained on these three artificial standards have been used to calculate the concentration in doped chrysotiles. Standard deviations are in the following ranges: 0.2–1.5% for Li and As, 0.2 to 1.2% for Sb and Cs. detection limits are ≈50 ng g^{-1} for Sb and Cs and ≈200 ng g^{-1} for Li and As. The trace element concentrations in equilibrium fluids [(as)] were deduced from the content weighed for the starting solution and the concentration measured at the end of the experiment in experimental product [(ctl)].

Boron concentrations were determined at the Laboratoire d'Hydrologie et de GEochimie de Strasbourg (LHyGeS) by ICP-MS using a Thermo Finnigan X series II. Since acid digestion using HF leads to a significant B loss through the formation of the volatile BF_3 compound, the classical procedure of rock acid digestion is precluded. Instead, about 50 mg of crushed sample were mixed in a Pt-Au crucible with about 250 mg of K_2CO_3 and heated at 950 °C for 15 min. The fusion residue was then dissolved using ultrapure water (18.2 MΩ) followed by a 15 min centrifugation at 4,000 rpm. The sample solutions were then analyzed without purification. Concentrations were determined using the ^{10}B ion beam because of the possible overlap of the large ^{12}C ion beam (inherited from the alkali fusion) with ^{11}B. The B calibration solutions were prepared using a K_2CO_3 solution representative of the sample chemical matrix. The full protocol for treatment and measurements are described in [40,41]. Repeated analyses of standard and sample solutions offered a long-term analytical reproducibility of 5% (±2σ, $n = 15$).

3. Results and discussion

3.1. Chrysotile textural properties

Specific surface area

N_2 sorption isotherms measurements (Fig. 1) for both undoped and doped chrysotile systematically suggest that they are mesoporous materials. The pore size is always between 2 and 50 nm with a median value between 4 and 22 nm, as determined by BJH method. Unlike undoped chrysotile ($S_{BET} \approx 184$ m^2 g^{-1}, [35], doped chrysotile shows significant variations of calculated specific

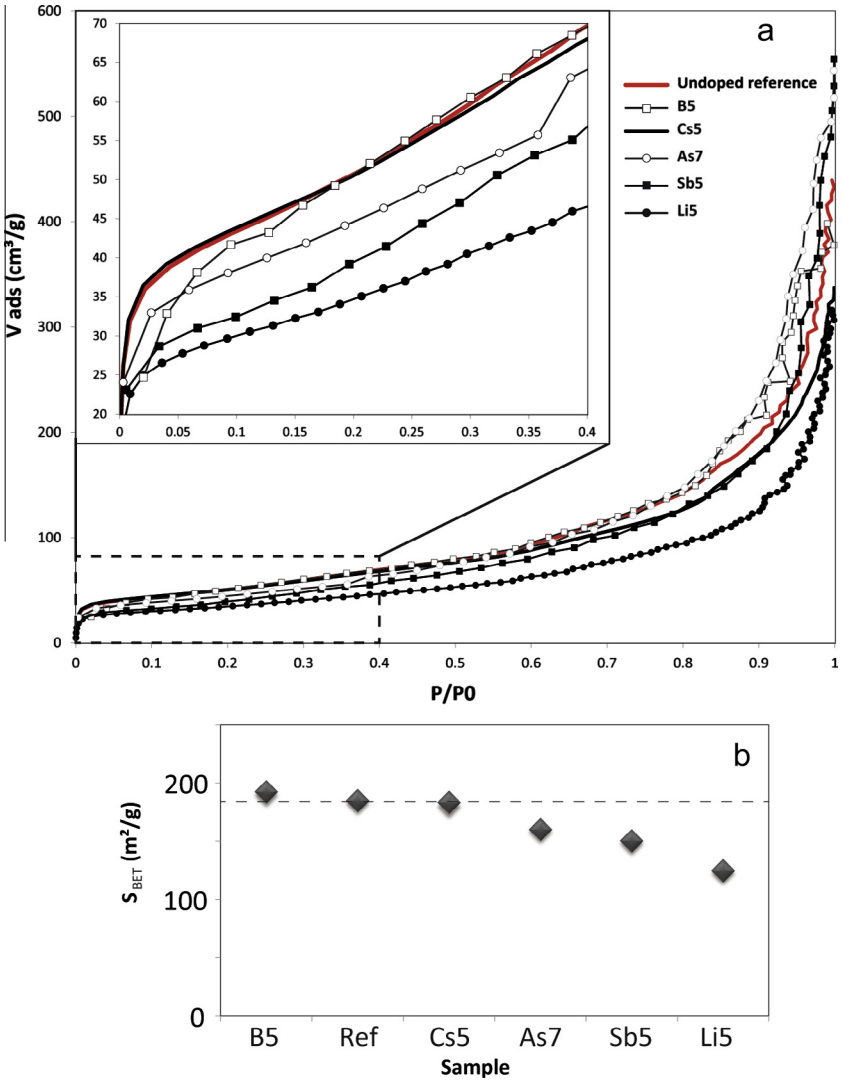

Fig. 1. (a) N_2 adsorption isotherms for doped synthetic chrysotiles, focus on $0 < P/P_0 < 0.4$ range, undoped reference [35] is represented in red, note the steeper slope of the curve for the B5 sample indicating higher specific surface area and (b) calculated specific surface area (S_{BET}) deduced from these isotherms.

surface area (Fig. 1b and Table 1). Li- and Sb-doped chrysotiles are characterized by a lower specific surface area S_{BET} (125 $m^2 g^{-1}$ and 150 $m^2 g^{-1}$, respectively for runs Li5 and Sb5).

Conversely, B-doped chrysotile has a slightly higher specific surface area (S_{BET} = 196 $m^2 g^{-1}$ and 191 $m^2 g^{-1}$, B2 and B5 samples). The specific surface area of As-doped chrysotile is comparable to that of the reference chrysotile except for the most As-doped sample (run As7) which has a lower specific surface area of 160 $m^2 g^{-1}$. For Cs-doped samples, measured specific surface areas are systematically similar to the S_{BET} of undoped the chrysotile reference.

Whatever the experiment the hysteresis loop between sorption and desorption branches did not close completely until the relative pressure P/Po had returned to 0.2 indicating a broad distribution of the pore size. This observation was confirmed by calculations from the N_2 desorption branch using the BJH model indicating that all samples are characterized by a broad distribution of the pore size (Table 1). Yet, no clear relationship was observed for the trace elements considered here.

Crystal morphology

FESEM and TEM observations show that each trace element have different effects on the morphology of chrysotile. FESEM-based measurements indicate that the typical size of undoped chrysotile nanotubes synthesized in our system were ≈15.45 nm in width (Table 2) with variable lengths, from 100 nm to 800 nm.

It has been reported in the literature that the presence of seeds, impurities or dissolved minor elements (e.g., Fe, Ni, Co) can affect the growth of chrysotile and induce crystallographic perturbation. This may occur via sorption and/or incorporation of impurities within the growing crystal surfaces thereby modifying the growth processes [24,29] by inhibiting or promoting mineral growth along different crystallographic orientations.

The presence of impurities can also lead to the formation of clusters and then affect the phase stability as well as the reaction kinetics for nanoparticles formation. As a result, chrysotile fibers synthesized in the presence of minor elements feature various complex morphologies (cylinder in cylinder, cone-in-cone etc., [26,28]. Moreover, we suggest that cationic substitutions affect the structure of chrysotile.

Here, we stress that small amounts of trace elements induce perturbations on chrysotile growth and result in complex chrysotile morphologies. Fig. 2 and Table 2 show the repartition of nanoparticle widths for the most trace element-doped chrysotiles and width parameters for a minimum of 200 fibers for each synthesis on several TEM micrographs and complementary FESEM micrographs. We clearly see that Cs and B do not affect particle width distributions contrary to Li, Sb and As to a lesser extent which favors the formation of >20 nm width cylinder in cylinder nanotubes (Fig. 2). Compared to undoped chrysotile (Fig. 3a), heterogeneous particles were observed for Li-, Sb-, and As-doped chrysotile experiments (Fig. 3b, c and d). In the Li- and Sb-doped experiments, we also observed an assemblage dominated by stocky, sub-micrometric nanotubes with cylinder-in-cylinder morphologies mixed with single thin nanotubes and lizardite-like flat serpentine with edge curved flake morphology (Figs. 3d and 4). Li-doped chrysotiles present some defects due to degradations during sample preparation and/or alteration under the beam. As-doped experiments are dominated by fibers (~15 nm in width) mixed with cylinder in cylinder nanotubes that do not exceed 46 nm in width (Table 2). Typical nanotube widths observed by TEM correspond to successive 12–16 nm, 17–22 nm, 30–35 nm and 42–50 nm and exceptionally > 50 nm width cylinder in cylinder imbrications. Hence, we measured a higher chrysotile nanotube average width for Li-, Sb-, and As-doped experiments (Table 2).

The large varieties of nanotubes and the presence of flat serpentine reflect the strong effect of trace element on chrysotile nucleation and growth. It also results in the formation of a more heterogeneous material compared to undoped chrysotile. Nevertheless, no nanotubes with diameters greater than 100 nm and polygonal structures [42] were observed. Moreover, proto-chrysotile and cone-in-cone morphologies were not observed in these experiments (all with reaction duration of 30 h). However, proto-chrysotile was clearly observed before 2 h of reaction in our previous study [35] dealing on the nucleation and growth processes of chrysotile.

We note that nanoscale observations are in good agreement with macroscopic results (S_{BET}). Li-doped, Sb-doped and most As-doped chrysotile samples feature a higher proportion of thick particles resulting in a lower specific surface area (Fig. 1). Moreover, the observation of flat-serpentine after 30 h of reaction means that the sequestration of Li, Sb (Fig. 4a and b, respectively) and, to a lesser extent, As by chrysotile clearly affects the crystallization of serpentine with flat structures. In other words, our results suggest that Li, Sb and As stimulate the growth of nanotubes perpendicularly to the elongation axis.

Cs has no visible effect on the morphology of synthetic chrysotile particles (Fig. 5a). We therefore suspect that Cs has no effect on chrysotile nucleation and growth processes. This leads to similar S_{BET} and crystal width for Cs-doped experiments and the undoped chrysotile reference (Table 2).

As for boron, low concentrations ($[(ctl)] \approx 20\ \mu g\ g^{-1}$ and $[(aq)] \approx 50\ \mu g\ g^{-1}$) favors the growth of chrysotile along the c-axis and hence results in longer (up to 3 μm) fibrous chrysotile with a typical average width of 15 nm (Fig. 6b and Table 2) (unlike Li, Sb and As which promote mineral growth along the c-axis). Occasionally however, larger 30 nm wide nanotubes have been observed (Fig. 6b). Yet we did not notice thick fibers as in the case of Li-doped experiments (Fig. 5c). The formation of thin micrometric-fibers is consistent with a specific surface area close to that of undoped-chrysotile wherein nanotubes lengths never exceed 1 μm. As reported in Table 1 the median pore size deduced from

Table 1
Specific surface area, cumulative pore volume, and median pore size for experimental products.

Sample	S_{BET} ($m^2 g^{-1}$)	Pore volume ($cm^3 g^{-1}$)	Medianpore size (nm)
Ref	184.8	0.64	21.6
Li2	160.2	0.38	15.8
Li5	124.8	0.47	19.6
Cs2	177.7	0.47	16.7
Cs5	181.8	0.46	16.3
As2	186.6	0.59	16.0
As5	194.1	0.67	9.1
As7	160.1	0.79	17.6
B2	196.3	0.42	4.4
B5	191.6	0.60	13.5
Sb2	185.4	1.04	21.8
Sb5	150.2	0.78	21.6

Table 2
Summary of minimum (min), maximum (max) and average width of nanotubes and morphologies observed for different runs, c-in-c for cylinder-in-cylinder.

Run.	Nanotube width (nm)			Morphology
	Size min	Size max	Average size	
REF	9.4	21.9	15.15	Fiber
Cs5	9.5	27	15.45	Fiber
B5	9.8	31.8	15.44	Fiber
Li5	11	92.8	23.9	c-in-c > fiber > flat
Sb5	8.8	51.3	24.9	c-in-c > fiber > flat
As7	10.1	45.8	19.8	Fiber > c-in-c

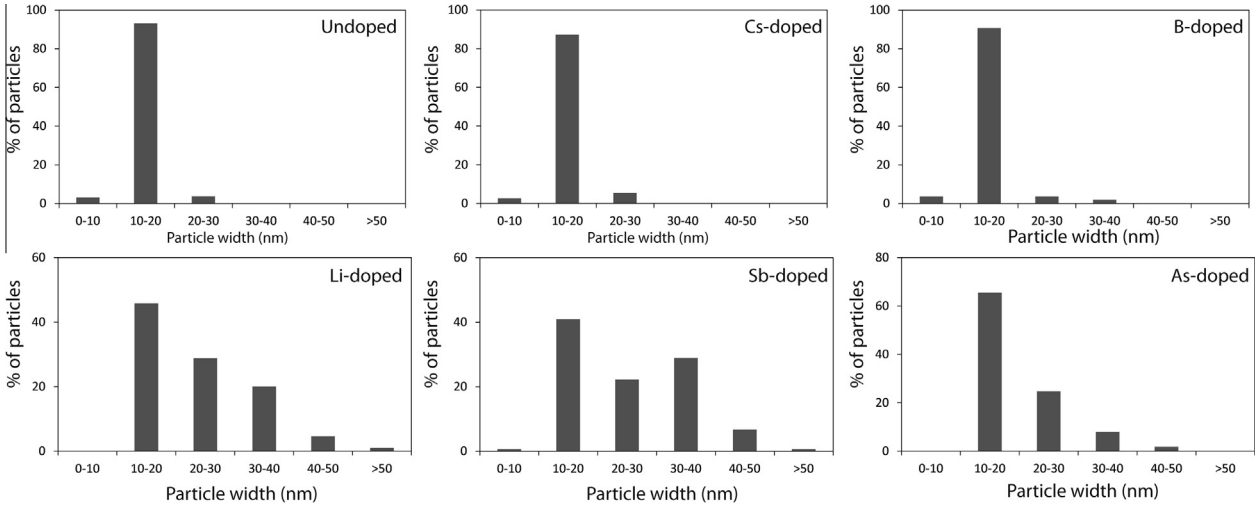

Fig. 2. Histograms representing the frequency of particles outer diameter (in nm) in undoped synthetic chrysotile runs and from most trace-element-doped runs: run Cs5, B5, Li5, Sb5 and As7.

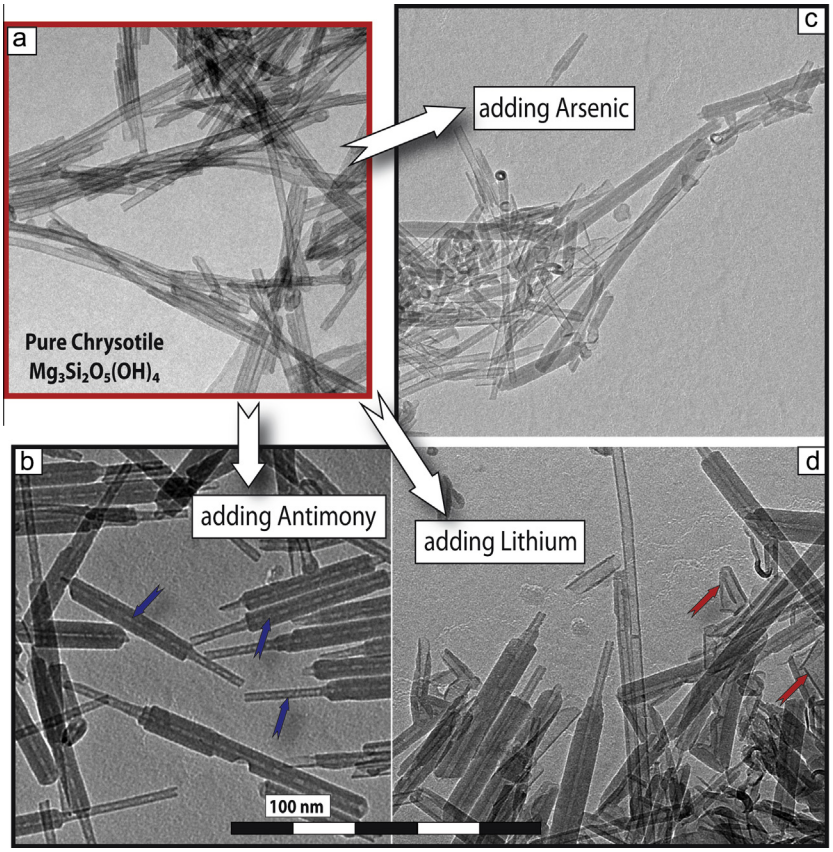

Fig. 3. Transmission electron micrographs of undoped synthetic chrysotile (a) compared to (b) Li-doped chrysotile (Li5), (c) As-doped chrysotile (As7) and (d) Sb-doped chrysotile (Sb5) and flat serpentine (indicated by red arrows). Blue arrows indicate nanotubes characterized by discontinuous core channel. (For interpretation of the references to colour in this figure legend, the reader is referred to the web version of this article.)

the BJH method is lower for B-doped sample (13.5 nm) with respect to the undoped reference (21.6 nm). This textural change can explain a slight increase of specific surface area.

Trace element sequestration, even at low concentrations, significantly affects the textural properties of synthetic chrysotile nanotubes. Macroscopic observations (specific surface area, Fig. 1) are consistent with nano- and micro-scale observations (morphology, Figs.3 and 4–6). We have no clear information regarding the mechanisms of trace element sequestration during chrysotile formation. Nevertheless considering that all our samples were carefully washed, we rejected adsorption as a possible explanation. The SEM mapping (Fig. 7) revealed a homogeneous distribution of Sb. This suggests a simple incorporation and/or substitution of trace elements within interlayers. Mg and/or Si substitutions can be evoked for Sb and As trapping due to their similar ionic radius (54 pm for Si, 86 pm for Mg, 60–72 pm for As and 74–90 pm for

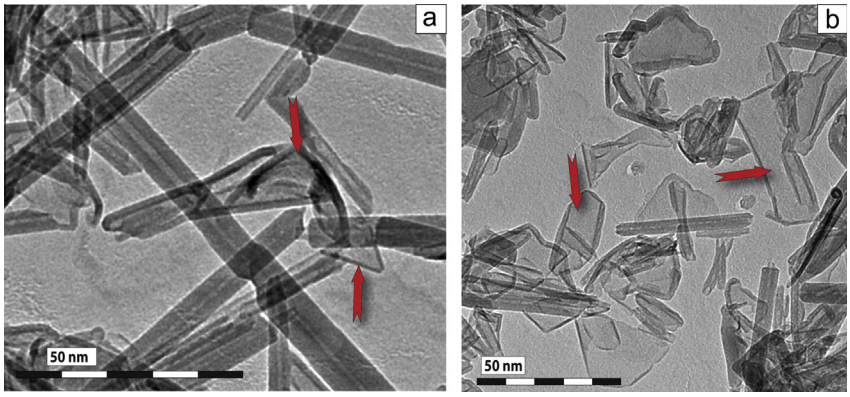

Fig. 4. Transmission electron micrographs of synthetic chrysotile and flat serpentine (indicated by arrows), (a) Li-doped chrysotile (Li5) and (b) Sb-doped chrysotile (Sb5).

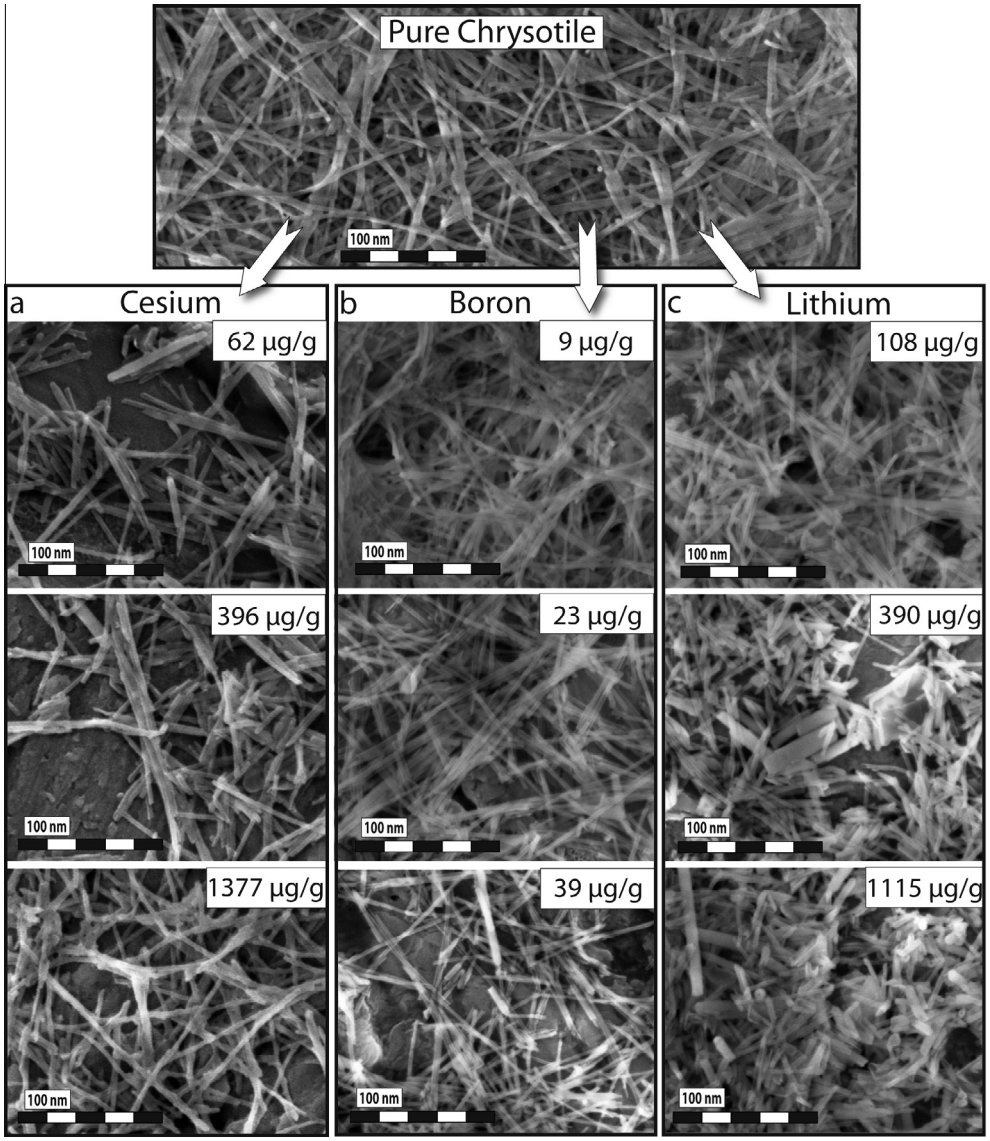

Fig. 5. Scanning electron microscope imaging of undoped synthetic chrysotile, and with samples, respectively doped from top to bottom with (a) 62, 396 and 1377 µg g^{-1} of cesium (Cs1, Cs3, Cs5), (b) 9, 23, 39 µg g^{-1} of boron (B1, B3, B4) and (c) 108, 390 and 1115 µg g^{-1} of lithium (Li2, Li3, Li5). Note the transition from homogeneous nanotubes to stockier particles in the presence of lithium, and the evolution to longer particles despite a very low boron concentration. Cesium has no influence on the size and morphologies of synthetic chrysotile.

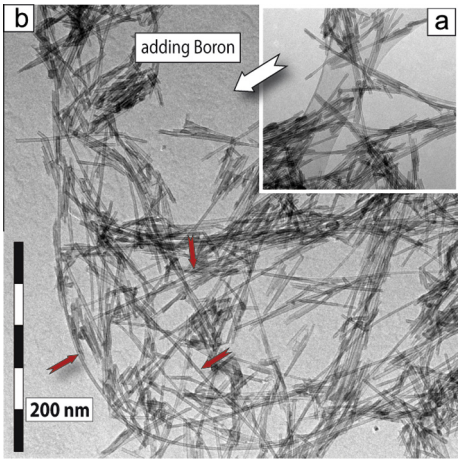

Fig. 6. Transmission electron micrograph of synthetic chrysotile, (a) undoped chrysotile and (b) B-doped chrysotile (B5), micrometric fibrous chrysotiles are indicated by arrows.

Sb, [43]). Moreover, it has been shown that octahedral Li-Mg substitution can occur for other clay minerals (e.g., smectite [44]). The hollow center of the nanotubes could also act as an ideal trapping location [32] for elements with large ionic radius (in our case, Li and Cs).

Thermal analyses of chrysotile

All TGA for trace-element-doped samples, performed from 30 °C to 1200 °C, are characterized by a continuous weight loss of about 12 wt% from 400 °C to 700 °C due to chrysotile déhydroxylation [35]. Despite the low trace element concentrations, some TGA changes can be observed. For As-, Li- and B-doped chrysotile, the endothermic peak decomposition is shifted to lower temperature (600 °C) compared with undoped chrysotile (607 °C, Table 3, Fig. 8). Cationic-substitution of dopant and/or the presence of trace element as impurity could explain this shift as it has been reported that both major and minor element substitutions [22,28] as well as the presence of seeds systematically induce a shift of the endothermic peak for chrysotile destabilization to lower temperature with respect to pure material. Following these results, we suggest that the thermal shifts observed here could be related to the presence of trace elements "impurities" in the system (at concentrations ranging from 65 to 2650 μg/g for the most doped experiments). Moreover, Sb-bearing impurities were detected by TEM. In the same way, lizardite crystals made of brucitic layers are characterized by lower dehydroxylation temperatures compare to chrysotile

Table 3
Differential thermal analyses results for synthetic chrysotile nanotubes.

Sample	DTA pic (°C)	
	Endo	Exo
REF	606.7	827
As7	599.7	823
B5	599.7	815.7
Li5	600.3	817.7
Cs5	609	816.3
Sb5	611	823

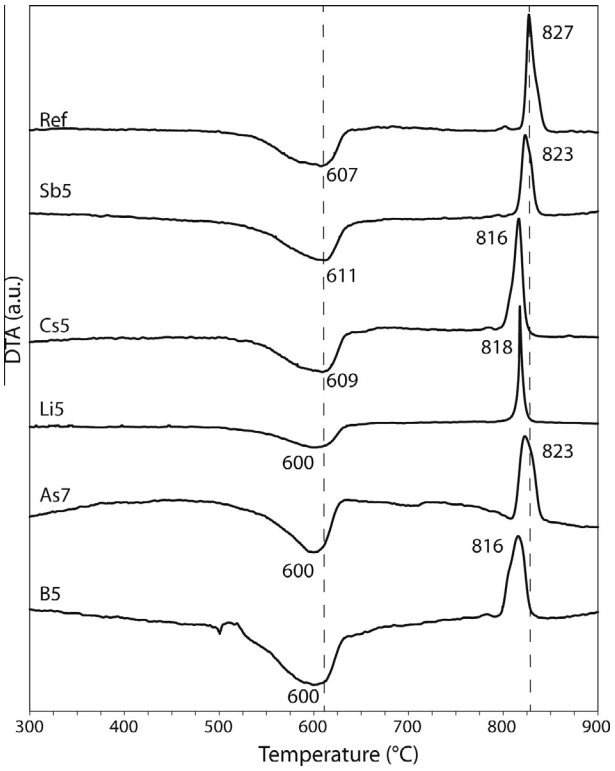

Fig. 8. DTA curves for undoped (Ref) and highest trace-element-doped experiments.

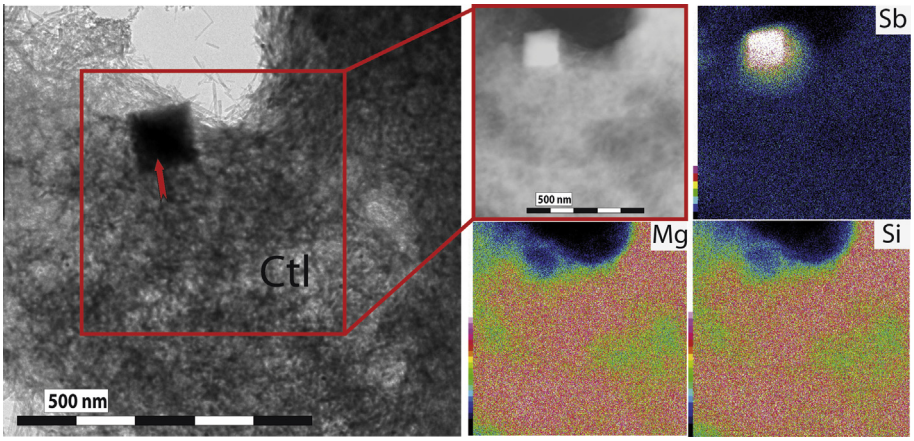

Fig. 7. Example of transmission electron micrographs and SEM mapping for Sb, Mg and Si element for run Sb5. The presence of Sb-rich impurity is indicated by arrow.

[45]. Indeed, the formation of flattened serpentine (Fig. 4) for As- and Li-doped syntheses is consistent with a shift towards a lower dehydroxylation temperature.

Sb-doped chrysotile thermal analysis shows a slight shift to higher temperatures (611 °C). This perturbation of the DTA signal may be a consequence of the presence of a large proportion of wide cylinder-in-cylinder particles compare to pure chrysotile. Finally, the DTA curve of Cs-doped chrysotile (609 °C) is similar to that of Sb-doped experiments.

For all our samples, the exothermic peak related the crystallization of forsterite[38] is systematically shifted towards lower temperature. This thermal effect could be due to the presence of the trace elements as impurities affecting the re-crystallization of forsterite.

3.2. Partitioning of trace elements

Trace elements in fluid and solid experimental products have been analyzed by ICP-MS for all the hydrothermal syntheses (Fig. 8, Table 4). Trace element concentrations in bulk serpentine show large variations: 20–1115 μg g^{-1} for Li, 9–65 μg g^{-1} for B, 60–1400 μg g^{-1} for Cs, 20–2650 μg g^{-1} for Sb and 20–1530 μg g^{-1} for As.

In our system, the amount of ions or molecules removed from the solution under equilibrium [(ctl)] depends of the equilibrium concentration of the fluid [(aq)]. Several empirical or mechanistic models (e.g., Langmuir, Freundlich, Brunauer–Emmett–Teller, and others) can be used to correlate and describe the processes behind ion removal. These removal models include all the mechanisms of adsorption, substitution or co-precipitation during mineral crystallization from aqueous solutions. The partitioning of trace elements in our system can be expressed as: $[(ctl)] = f[(aq)]$,

We modeled sequestration isotherms for each trace element from our experimental data using the Langmuir equation (Fig. 9).

This approach is commonly used to calculate the potential of one mineral to remove one element/molecule in the solution (e.g., [46]). In our system, the Langmuir equation can be written as:

$$[(ctl)] = \frac{[(ctl)]_{max} K_L [(aq)]}{1 + K_L [(aq)]} \quad (1)$$

where $[(ctl)]_{max}$ is the maximum amount of trace element removed to reach the saturation state [mg g^{-1}] and K_L is the Langmuir coefficient. $K_L[(aq)]$ can be interpreted as the equilibrium trace-element removal coefficient in [L mg^{-1}] and expressed as:

$$K_L = \frac{K_D}{[(ctl)]_{max}}. \quad (2)$$

This allowed us to calculate K_D [L g^{-1} or ml g^{-1}], which is the liquid–solid distribution coefficient:

$$K_D = K_L * [(ctl)]_{max} \quad (3)$$

This physicochemical parameter is then used to determine the geochemical element-transfer. Both K_D and $[(ctl)]_{max}$ were obtained by fitting our experiments with a nonlinear regression following the least squares method (Table 5).

The removal processes are more intricate for the As-, Li- and Sb-doped experiments within the range of concentrations tested. The one-site saturation models proposed by Langmuir isotherms are not sufficient to fit the experimental data over the whole concentration range. The effect of secondary removal processes is not considered. In our experiments, we observed that at the highest concentrations, As-, Li- or Sb-doped samples displayed higher measured concentrations than those predicted $[(ctl)]_{max}$ using the Langmuir model based on lower concentrations (Fig. 9). These drifts could be explained by the precipitation of secondary microphases due to trace element supersaturation concentrations in the solution. This assumption was independently confirmed by microscopic observations (TEM) on the highly Sb-doped sample (Sb5)

Table 4
Li, B, Cs, Sb and As contents of experimental solid phases [(Ctl)] and solutions [(aq)] for the 30 h chrysotile syntheses and corresponding partitioning coefficient calculated between chrysotile and solution.

Sample	Chrysotile synthesis content (μg/g)					Solution content (μg/g)						Relative partition coeff. (*)
	Li	B	Cs	Sb	As	Initial	Li	B	Cs	Sb	As	
Li1	21.6	–	–	–	–	5.1	5.7	–	–	–	–	3.77
Li2	108.2	–	–	–	–	20.0	12.2	–	–	–	–	8.84
Li3	251.4	–	–	–	–	49.5	47.2	–	–	–	–	5.33
Li4	389.8	–	–	–	–	99.9	102.3	–	–	–	–	3.81
Li5	1115.7	–	–	–	–	201.3	189.0	–	–	–	–	5.90
B1	–	9.3	–	–	–	5.1	–	5.0	–	–	–	1.86
B2	–	13.1	–	–	–	19.3	–	19.1	–	–	–	0.68
B3	–	23.2	–	–	–	49.7	–	49.5	–	–	–	0.47
B4	–	38.8	–	–	–	98.9	–	98.5	–	–	–	0.39
B5	–	65.6	–	–	–	200.2	–	199.6	–	–	–	0.33
Cs1	–	–	61.7	–	–	5.1	–	–	4.6	–	–	13.53
Cs2	–	–	156.3	–	–	20.3	–	–	18.8	–	–	8.30
Cs3	–	–	396.9	–	–	50.2	–	–	46.5	–	–	8.53
Cs4	–	–	750.4	–	–	100.2	–	–	93.3	–	–	8.04
Cs5	–	–	1377.0	–	–	198.8	–	–	186.2	–	–	7.39
Sb1	–	–	–	24.0	–	5.6	–	–	–	5.4	–	4.45
Sb2	–	–	–	102.0	–	20.3	–	–	–	19.3	–	5.27
Sb3	–	–	–	238.8	–	51.8	–	–	–	49.6	–	4.81
Sb4	–	–	–	1714.2	–	111.7	–	–	–	96.0	–	17.86
Sb5	–	–	–	2654.3	–	213.5	–	–	–	189.2	–	14.03
As1	–	–	–	–	22.4	5.2	–	–	–	–	5.0	4.46
As2	–	–	–	–	43.1	20.0	–	–	–	–	19.5	2.21
As3	–	–	–	–	133.9	50.0	–	–	–	–	48.7	2.75
As4	–	–	–	–	273.6	99.6	–	–	–	–	97.1	2.82
As5	–	–	–	–	499.4	199.9	–	–	–	–	195.4	2.56
As6	–	–	–	–	579.8	508.1	–	–	–	–	503.0	1.15
As7	–	–	–	–	1527.2	1011.4	–	–	–	–	998.0	1.53

(*)Relative partition coefficient = [(Ctl)]/[(aq)].

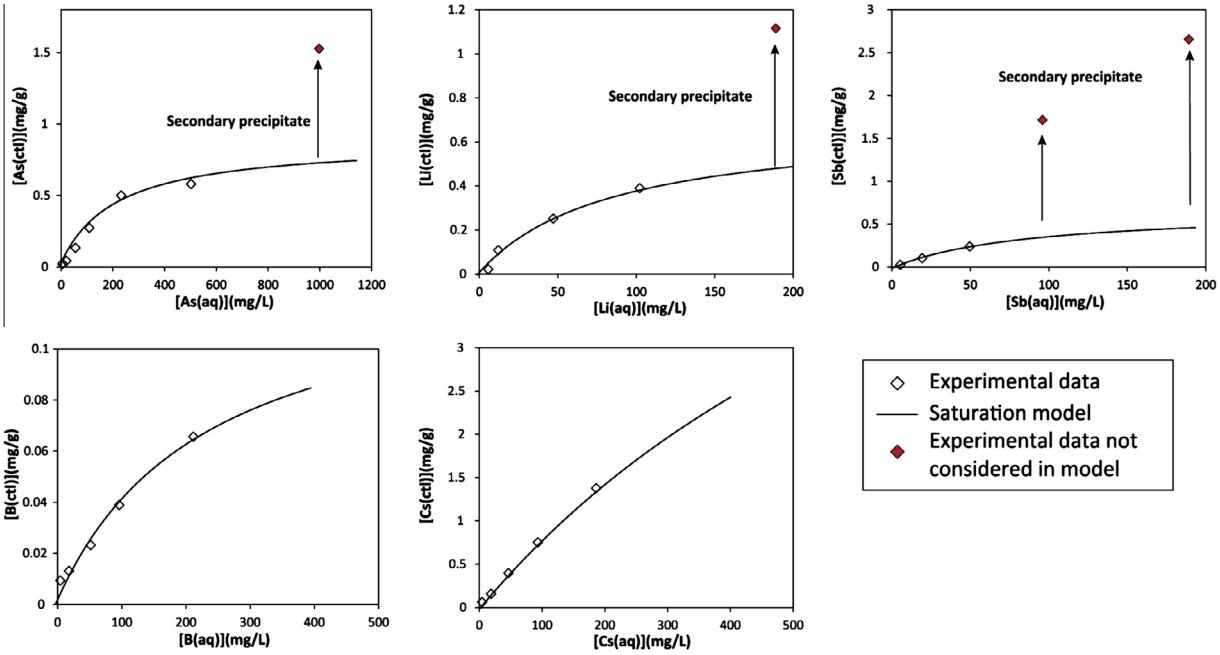

Fig. 9. Trace element concentrations in synthetic chrysotile [(ctl)] after 30 h of reaction at 300 °C as a function of trace element concentrations in calculated equilibrium solutions [(aq)] and corresponding one site saturation models.

Table 5
Partition parameters for calculation of trace-element removal isotherms by using Eq. (1).

Element	K_D ml/g	$[(ctl)]_{max}$ mg/g
Li	8.46	0.705
B	0.58	0.135
Cs	8.86	8.3
As	4.09	0.9
Sb	7.33	0.660

that shows the presence of Sb-rich microphases (Fig. 7). Despite the precipitation of secondary phases, SEM mapping indicates that Sb is homogeneously distributed in chrysotile, suggesting a substantial Sb sequestration of by the latter.

For these reasons, only low concentration samples were considered for the Langmuir model calculation and high concentration samples (runs Li5, Sb4, Sb5 and As7) were not used to calculate trace-element removal isotherms (Fig. 9).

The results are very different depending of the considered trace element. Calculated $[(ctl)]_{max}$ and K_D are, respectively of 0.135 mg g^{-1} and 0.58 ml g^{-1} for B, 0.705 mg g^{-1} and 8.46 ml g^{-1} for Li, 0.9 mg g^{-1} and 4.09 ml g^{-1} for As, 8.3 mg g^{-1} and 8.86 ml g^{-1} for Cs and 0.660 mg g^{-1} and 7.33 ml g^{-1} for Sb (Table 4). The result for boron is particularly surprising as it is known that this element is relatively abundant (10–100 μg g^{-1} e.g., [47]) in natural abyssal serpentinites [48] formed after the alteration of peridotite reacting with seawater and/or hydrothermal fluids (≈5 μg g^{-1} of B) [49]. This could be due to the particularly high pH conditions.

From our TEM analyses, we noticed that undoped chrysotile is characterized by the absence of contrast in the core of the nanotubes (Figs. 3 and 6a). It is also the case for Cs-, Li, As- and B- doped chrysotiles. These observations suggest that the core channels of nanotubes are empty. On the other hand, Sb-doped nanotubes are characterized by discontinuous channel cores (Fig. 3b) highlighting a density contrast. We therefore suspect that Sb is trapped into chrysotile individual nanotubes and cylinder-in-cylinder nanotubes core cavities.

4. Conclusion

The influence of single fluid mobile elements on chrysotile textural properties has been measured from macroscopic (N_2 sorption isotherms) to nanometer scale (TEM, FESEM). Variations of particle size and morphology of crystal faces were determined as a function of the trace elements considered and/or trace element contents in the synthetic chrysotile. Compared to our reference, Sb, As and particularly Li favor the formation of wider chrysotile particles with typical cylinder in cylinder morphology up to 50 nm in width, leading to a lower specific surface area. These particles co-precipitate with flat edge curved serpentines. Despite a low solid-solution partition coefficient (K_D = 0.58 ml g^{-1}), B sequestration favors the formation of longer nanotubes with an average width similar to undoped chrysotile (14 nm). Cs has no effect on chrysotile textural properties.

On the other hand, the solid–liquid partition coefficient of Li, B, As, Sb and Cs were determined using a single saturation site model (Langmuir equation). These new data have been obtained at 300 °C in alkaline hydrothermal conditions. The results vary from 0.58 for B to 8.86 ml g^{-1} for Cs.

These results have great implications to improve the understanding of the role of trace elements on the serpentinization processes from oceanic ridges to subduction environments This study also presents some interesting outcomes for societal applications such as asbestos reactivity or CO_2 sequestration. For instance, it means that during the serpentinization process, the partitioning differs from one element to the other. This has to be considered for volatile elements recycling in subduction zones. Moreover, boron could be used to favor/stimulate the growth of nanotubes along the elongation-axis. This surprising behavior is contrary to classic growth inhibition in chrysotile minerals.

Acknowledgements

The authors would like to thank the French National Center for Scientific Research (CNRS) and the Université Joseph Fourier (UJF) in Grenoble for providing financial support. R. Lafay was supported by a Ph.D Grant from French ministry of research. The authors are

very grateful to O. Vidal, whom allowed us to use a sophisticated autoclave to perform various experiments and to C. Chauvel and C. Poggi for their help with the ICP-MS measurements and data treatment.

References

[1] E.J.W. Whittaker, Acta Crystallogr. 8 (1955) 571–574.
[2] K. Yada, Acta Crystallogr. Sect. 27 (1971) 659–664.
[3] G. Cressey, B.A. Cressey, F.J. Wicks, K. Yada, Mineral. Mag. 74 (2010) 29–37.
[4] E. Whittaker, Acta Crystallogr. 10 (1957) 149–156.
[5] E. Whittaker, Acta Crystallogr. 9 (1956) 855–862.
[6] E. Whittaker, Acta Crystallogr. 9 (1956) 862–864.
[7] E. Whittaker, Acta Crystallogr. 9 (1956) 865–867.
[8] A. Baronnet, B. Devouard, Can. Mineral. 43 (2005) 513–542.
[9] K. Yada, W. Liu, Sixth Meet Eur. Clay Group Seville Spain, 596 (1987).
[10] W.E. Seyfried Jr., W.E. Dibble Jr, Geochim. Cosmochim. Acta 44 (1980) 309–321.
[11] W.W. Wegner, W.G. Ernst, Am. J. Sci. 283A (1983) 151–180.
[12] F.J. Wicks, E.J.W. Whittaker, Can. Miner. 15 (1977) 459–488.
[13] B. Evans, Int. Geol. Rev. 46 (2004) 479–506.
[14] F. Larachi, J.-P. Gravel, B.P.A. Grandjean, G. Beaudoin, Int. J. Greenhouse Gas Control 6 (2012) 69–76.
[15] P. Sabatino, L. Casella, A. Granata, M. Iafisco, I.G. Lesci, E. Monzani, N. Roveri, J. Colloid Interface Sci. 314 (2007) 389–397.
[16] E. Foresti, E. Fornero, I.G. Lesci, C. Rinaudo, T. Zuccheri, N. Roveri, J. Hazard. Mater. 167 (2009) 1070–1079.
[17] E. Korytkova, A. Brovkin, T. Maslennikova, L. Pivovarova, I. Drozdova, Glass Phys. Chem. 37 (2011) 161–171.
[18] B. Jancar, D. Suvorov, Nanotechnology 17 (2006) 25–29.
[19] A. Bloise, E. Belluso, J. Am. Ceram. Soc. 95 (2012) 3050–3055.
[20] E.N. Korytkova, A.V. Maslov, L.N. Pivovarova, Y.V. Polegotchenkova, V.F. Povinich, V.V. Gusarov, Inorg. Mater. 41 (2005) 743–749.
[21] M. Andreani, A. Baronnet, A.-M. Boullier, J.-P. Gratier, Eur. J. Mineral. 16 (2004) 585–595.
[22] A. Bloise, E. Belluso, E. Barrese, D. Miriello, C. Apollaro, Cryst. Res. Technol. 44 (2009) 590–596.
[23] M. Bentabol, M.D. Ruiz Cruz, F.J. Huertas, Appl. Clay Sci. 42 (2009) 649–656.
[24] A. Bloise, E. Barresse, C. Apollaro, Neues Jahrb. Für Miner. -Abh. 185 (2009) 297–304.
[25] E. Korytkova, L. Pivovarova, Glass Phys. Chem. 36 (2010) 53–60.
[26] A. McDonald, B. Scott, G. Villemure, Microporous Mesoporous Mater. 120 (2009) 263–266.
[27] G. Falini, E. Foresti, G. Lesci, N. Roveri, Chem. Commun. (2002) 1512–1513.
[28] E. Foresti, M.F. Hochella, H. Kornishi, I.G. Lesci, A.S. Madden, N. Roveri, H. Xu, Adv. Funct. Mater. 15 (2005) 1009–1016.
[29] A. Bloise, E. Belluso, E. Fornero, C. Rinaudo, E. Barrese, S. Capella, Microporous Mesoporous Mater. 132 (2010) 239–245.
[30] E. Korytkova, L. Pivovarova, V. Gusarov, Geochem. Int. 45 (2007) 825–831.
[31] B.A. Cressey, E.J.W. Whittaker, Mineral. Mag. 57 (1993) 729–732.
[32] B. Wunder, F. Deschamps, A. Watenphul, S. Guillot, A. Meixner, R. Romer, R. Wirth, Contrib. Mineral. Petrol. 159 (2010) 781–790.
[33] F. Deschamps, S. Guillot, M. Godard, M. Andreani, K. Hattori, Terra Nova 23 (2011) 171–178.
[34] K. Hattori, S. Guillot, Geology 31 (2003) 525–528.
[35] R. Lafay, G. Montes-Hernandez, E. Janots, R. Chiriac, N. Findling, F. Toche, Chem.-Eur. J. 19 (2013) 5417–5424.
[36] E.P. Barrett, L.G. Joyner, P.P. Halenda, J. Am. Chem. Soc. 73 (1951) 373–380.
[37] C. Chauvel, S. Bureau, C. Poggi, Geostand. Geoanal. Res. 35 (2011) 125–143.
[38] K. Govindaraju, Geostand. Newsl. 18 (1994) 1–158.
[39] K.P. Jochum, M. Willbold, I. Raczek, B. Stoll, K. Herwig, Geostand. Geoanal. Res. 29 (2005) 285–302.
[40] D. Lemarchand, D. Cividini, M.-P. Turpault, F. Chabaux, Geochim. Cosmochim. Acta 98 (2013) 78–93.
[41] D. Cividini, D. Lemarchand, F. Chabaux, R. Boutin, M.-C. Pierret, Geochim. Cosmochim. Acta 74 (2010) 3143–3163.
[42] A. Baronnet, B. Devouard, J. Cryst. Growth 166 (1996) 952–960.
[43] R. Shannon, Acta Crystallogr. A 32 (1976) 751–767.
[44] A. Decarreau, N. Vigier, H. Pálková, S. Petit, P. Vieillard, C. Fontaine, Geochim. Cosmochim. Acta 85 (2012) 314–325.
[45] M.K. Titulaer, J.C. van Miltenburg, J.B.H. Jansen, J.W. Geus, Clays Clay Miner. 41 (1993) 496–513.
[46] G. Montes-Hernandez, N. Concha-Lozano, F. Renard, E. Quirico, J. Hazard. Mater. 166 (2009) 788–795.
[47] F. Vils, L. Pelletier, A. Kalt, O. Müntener, T. Ludwig, Geochim. Cosmochim. Acta 72 (2008) 5475–5504.
[48] F. Vils, S. Tonarini, A. Kalt, H.-M. Seitz, Earth Planet. Sci. Lett. 286 (2009) 414–425.
[49] J. Charlou, J. Donval, Y. Fouquet, P. Jean-Baptiste, N. Holm, Chem. Geol. 191 (2002) 345–359.